RSC Advances

ROYAL SOCIETY OF CHEMISTRY

www.rsc.org/advances

Non-Enzymatic Hydrogen Peroxide Electrochemical Sensor Based on Three-Dimensional MnO_2 Nanosheets/Carbon Foam Composite

Shuijian He, [a,b] Boya Zhang, [a] Minmin Liu, [a,b] and Wei Chen *[a]

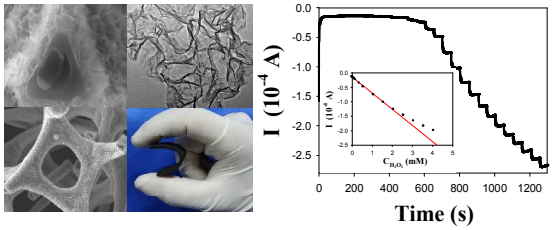

Three dimensional MnO_2 nanosheets/carbon foam has been fabricated and they exhibit promising electrochemical sensing performance for nonenzymetic H_2O_2 detection.

Cite this: DOI: 10.1039/c0xx00000x

www.rsc.org/xxxxxx

ARTICLE TYPE

Non-Enzymatic Hydrogen Peroxide Electrochemical Sensor Based on Three-Dimensional MnO_2 Nanosheets/Carbon Foam Composite

Shuijian He, [a,b] Boya Zhang,[a] Minmin Liu, [a,b] and Wei Chen*[a]

Received (in XXX, XXX) Xth XXXXXXXXX 20XX, Accepted Xth XXXXXXXXX 20XX
DOI: 10.1039/b000000x

A new type of three-dimensional electrochemical sensor platform, MnO_2 nanosheets/carbon foam (MnO_2/CF) hybrid nanostructure, was successfully fabricated for the nonenzymatic detection of H_2O_2. The morphology, structure and composition of the 3D nanostructures were systematically characterized by electron microscopy, X-ray diffraction and X-ray photoelectron spectroscopy. Uniform and thin MnO_2 nanosheets can be formed on the carbon foam after a simple chemical process by immersing carbon foam in $KMnO_4$ aqueous solution. The content of MnO_2 in the MnO_2/CF composites was found to play a great role in its sensing performance for H_2O_2 detection. The MnO_2/CF2 sample with a 24.5% MnO_2 content showed the best performance among the studied MnO_2/CF composites. The 3D hierarchical porous structure with thin MnO_2 nanosheets can provide enhanced electrochemically active surface area, high electrical conductivity and improved analyte diffusion, which makes it a promising electrochemical sensing platform. The electrochemical studies showed that the H_2O_2 sensor based on the MnO_2/CF2 exhibited excellent detection performance with a wide linear range from 2.5×10^{-6} to 2.055×10^{-3} M and a detection limit of 1.2×10^{-7} M (S/N = 3). These results demonstrate that such 3D nanocomposites have promising application in electrochemical sensors.

1. Introduction

H_2O_2 is one of the most important and widely used analytes in the electrochemical analysis, since it is a common oxidizing agent or an essential intermediate in biochemical, pharmaceutical, clinical, industrial and environmental fields. The precise and rapid detection of H_2O_2 is of significant importance. Owing to the high sensitivity and selectivity, electrochemical sensors based on the electrocatalysis of immobilized enzymes toward H_2O_2 are used widely.[1-3] However, due to the inevitable drawbacks of the enzymatic sensors such as instability, limited lifetime, high cost of enzymes, critical operating situation and complicated immobilization procedure, much effort has been devoted to the direct determination of H_2O_2 at non-enzymatic electrodes.[4-6]

Nowadays, metal and transition metal oxide nanoparticles have been applied extensively in fabricating highly efficient non-enzymatic electrochemical sensors.[7-11] Noble metallic nanostructures, like nanostructured Pt, Pd, Au, Ag and their alloys, are excellent candidate materials for the construction of non-enzymatic hydrogen peroxide sensors owing to their superior electrocatalytic activities.[12-17] However, the relatively high price and limited resources restrict their widely application. In recent years, much cheaper transition metal compound nanomaterials including CuO, CuS, Fe_3O_4, MnO_2, MoS_2, NiO and TiO_2, have been applied extensively in fabricating highly efficient non-enzymatic H_2O_2 sensors.[18-28] In particular, manganese dioxide nanomaterials are considered as one of the most appealing inorganic materials and have drawn attention in bioanalytical chemistry,[29, 30] especially in electrochemical sensing of H_2O_2, due to its low cost, natural abundance, environmental pollution-free and excellent catalytic activity which can promote H_2O_2 decomposition. Many kinds of MnO_2 nanomaterials have been utilized in the fabrication of H_2O_2 sensors.[31-33] However, due to intrinsic poor electric conductivity of MnO_2 (10^{-5}–10^{-6} S/cm), researchers tried to combine MnO_2 with various carbon materials like graphite,[34] graphene,[35] ordered mesoporous carbon,[36] carbon nanotube[37] and carbon nanofiber[38] to enhance the electric conductivity of MnO_2-based sensing materials.

Recently, 3D self-supported materials have been fabricated as platforms for electrochemical and gas sensors by modifying electrochemically active materials on 3D scaffolds, such as carbon/graphene foam, Ni foam and other substrates.[39-48] High detection performance with low detection limit, wide linear range and short response time has been achieved by these 3D material-based electrochemical sensors attributed to the large surface area, high electric conductivity and porous structure of the substrates and the high electrocatalytic performance of the electrochemically active materials. However, there are only a few reports on 3D non-enzymatic and non-noble metal H_2O_2 sensors. Xi et al. [49] reported that non-enzymatic sensors fabricated by thionine/polydopamine/graphene foams can detect H_2O_2 in a linear range from 0.4 to 660 μM. Zhang et al.[44] reported that a

linear range from 0.38 to 13.46 mM could be reached by a non-enzymatic sensor based on MnO_2/graphene foam. Both of the aforementioned materials showed their applications in non-enzymatic H_2O_2 sensor. Nevertheless, the preparation of graphene foam via chemical vapor deposition (CVD) using Ni foam as sacrificial template is complex, costly and time consuming. The output of graphene foam through CVD is also limited. So it is still a challenge to explore new types of 3D materials with easy preparation processes, large scale productivity and low cost for fabricating highly efficient non-enzymatic H_2O_2 sensors.

In this paper, flexible and porous carbon foam (CF) carbonized from low-cost commercial melamine resin foam was used as skeleton to fabricate non-enzymatic H_2O_2 sensor. After in-situ redox reaction with $KMnO_4$, a layer of MnO_2 nanosheets can grow epitaxially on the surface of carbon foam. The 3D sensors exhibited low detection limit, short response time, and wide linear range toward the detection of H_2O_2 which can be ascribed to the novel structure of MnO_2/CF composites. The porous structure of CF can not only provide the multiple electron paths, but also enable the efficient contact between the electrolyte and electrode surface, resulting in a rapid response to the analyte (H_2O_2). The large surface area of MnO_2 nanosheets offers plenty of contact area with H_2O_2 ensuring the low detection limit. The present study provides a new platform for nonenzymatic detection of H_2O_2.

2. Experimental Section

All the reagents used in the experiments were analytical grade and used without further purification. All aqueous solutions were prepared with ultrapure water (18.3 MΩ cm).

2.1 Preparation of carbon foam

Melamine resin foam (MRF, supplied by Puyang Green Universh Chemical Co., Ltd.) was carbonized in a tube furnace fixed with a quartz tube with 5 cm inner diameter under the protection of 100 mL/min Ar flow. Eight pieces of MRF with a size of 0.5 cm × 3.5 cm × 25 cm were piled up and put in the middle of the tube furnace. Carbonization temperature program was as follows. First, the temperature was raised from ambient temperature to 300 ^oC in 1 h and kept for 5 minutes. Second, the temperature was further raised to 400 ^oC in 100 minutes and kept for 5 minutes. Finally, the temperature was increased to 1000 ^oC in 5 h and kept for 1 h. The furnace was then cooled down to room temperature.

2.2 Fabrication of MnO_2/carbon foam composites (MnO_2/CF)

In order to improve the hydrophilicity of CF, CF was firstly wetted with ethanol and then washed with deionized water three times to remove residual ethanol. Without such a hydrophilicity process, the as-prepared CF can not be wholly infiltrated by $KMnO_4$ aqueous solution, resulting in nonuniform growth of MnO_2 nanosheets. A series of MnO_2/CF composites were prepared by varying the concentration of $KMnO_4$ aqueous solution from 0.5, 1, 2 and 3 to 5 mM. The composites were named as MnO_2/CF0.5, MnO_2/CF1, MnO_2/CF2, MnO_2/CF3 and MnO_2/CF5, respectively. In a typical synthesis of MnO_2/CF, 55 mg CF was dipped into 0.2 L $KMnO_4$ aqueous solution and the reaction was finished when the purple color of $KMnO_4$ disappeared. The reaction was conducted at 60 ^oC in a water bath.

2.3 Materials Characterization

Morphology of the samples was viewed by scanning electron microscopy (SEM; XL30) and transmission electron microscopy (TEM; Hitachi H-600). High-resolution TEM (HRTEM) images, X-ray energy dispersive spectroscopy (EDS) and the selected area electron diffraction (SAED) were carried out on a JEM-2010(HR) microscope. The crystal structures of the as-prepared products were characterized with an X-ray powder diffractometer (XRD; D/Max 2500 V/PC, Cu-Kα radiation). X-ray photoelectron spectroscopy (XPS) measurements were performed on a VG Thermo ESCALAB 250 spectrometer (VG Scientific) operated at 120 W with an energy analyzer working in the pass energy mode at 100.0 eV. An Al Ka line was used as the excitation source. The binding energy was calibrated against the carbon 1s line. The contents of MnO_2 in the composites were calculated from thermogravimetric analysis (TGA, Pyris Diamond TG/DTA) which was carried out under air flow of 60 mL min^{-1} with a heating rate of 5 ^oC/min.

2.4 Preparation of working electrodes and Electrochemical measurements

In order to preserve the novel 3D structure of MnO_2/CF composites, the working electrodes for H_2O_2 sensors were fabricated by cutting a piece of corresponding MnO_2/CF composites and pasting it on a graphite plate with conductive carbon adhesive. The graphite plate was connected to a stainless steel wire to facilitate the test. Other faces of the graphite plate were covered by epoxy resin to avoid their contact with solution, except the working face. The active materials were weighed on an electronic balance with the precision of 0.01 mg and the weights are between 0.1 and 0.2 mg. A CHI 660D electrochemical workstation (Shanghai, Chenhua) was used for all the electrochemical and impedance spectroscopy measurements with conventional three-electrode configuration using a graphite plate counter electrode and an Ag/AgCl reference electrode (saturated with KCl (aq)). The electrochemical sensing of H_2O_2 was carried out in 0.1 M phosphate buffer solution (PBS, pH=7.4) and the PBS was degassed with N_2 for 20 min before test.

3. Results and Discussion

3.1 Synthesis and characterization of materials

The morphology of the 3D nanomaterials was first characterized by electron microscopy. As showed in Fig. 1A, large-scale 3D nanostructures can be obtained with the present method, which is very favorable for the constructing electrochemical sensing platform. It should be noted that the performance of sensors based on nanoparticles may decrease with duty cycle increasing because of the aggregation of particles. The present rigid 3D nanomaterials, however, can provide very stable structure as sensing platform. It can be seen that the white melamine resin foam changed into grey carbon foam after carbonization. The colors of the MnO_2/CF composites become darker and darker with the increase of the concentration of $KMnO_4$ aqueous solution, which is ascribed to the increase of the thickness of MnO_2 layers (Fig. 2 and Fig. S1). It is noteworthy that all the as-prepared carbon foam and the MnO_2/CF composites retained the original foam-like structure of melamine resin foam. Fig. 1B-D

shows the SEM images of the prepared carbon foam at different magnifications. It can be seen that 3D carbon network with hollow structure was produced through the carbonization of melamine resin foam. As shown in Fig. 1 E-G, after the reaction between the carbon foam and $KMnO_4$ aqueous solution, uniform MnO_2 nanosheet layers were formed on the framework of the carbon foam. The foam-like materials are composed by triangle fibers which interconnected and formed plenty of micron-sized pores leading to network architecture.

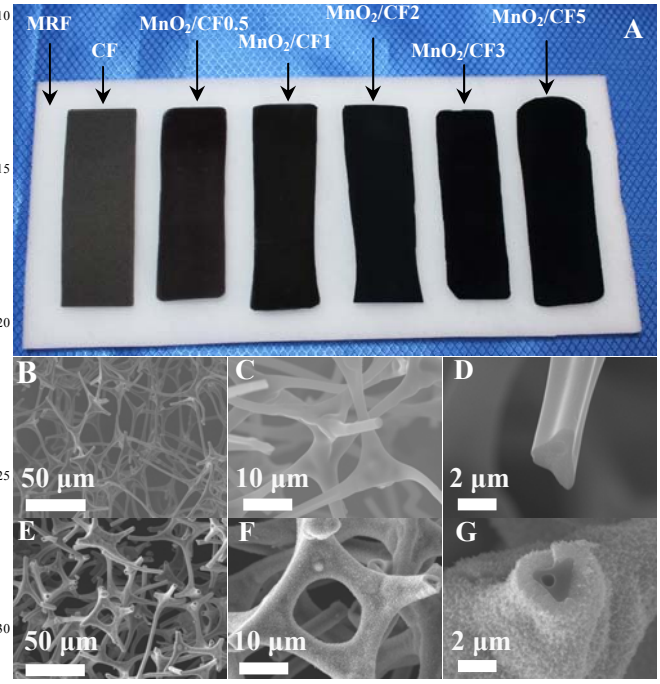

Fig. 1 (A) Digital photographs of melamine resin foam (MRF), carbon foam (CF) and the MnO_2/CF composites with different MnO_2 contents. (B-G) SEM images of CF (B, C, D) and MnO_2/CF3 (E, F, G) at different magnifications.

The effect of the $KMnO_4$ concentration on the structure of the MnO_2/CF composites was studied. Fig. 2 shows the SEM images of the MnO_2/CF structures produced from different $KMnO_4$ concentrations. From Fig. 2A, the carbon foam framework has a very smooth surface. After immersion of carbon foam in different concentrations of $KMnO_4$, all the surfaces of the 3D skeleton were covered by thin MnO_2 nanosheets. Interestingly, the size of the MnO_2 nanosheet and the thickness of the MnO_2 layers are strongly dependent on the concentration of $KMnO_4$. As shown in Fig. 2B-F, the MnO_2 nanosheets grow larger and larger with concentration of $KMnO_4$ below 2 mM. However, when the concentration of $KMnO_4$ further increases above 2 mM, the size of the produced MnO_2 nanosheets decreases gradually. This phenomenon can be ascribed to the rapid reaction between $KMnO_4$ and CF and the quick formation of small MnO_2 nucleus at the relatively high concentrations of $KMnO_4$. From the cross section view SEM images shown in Fig. 2 insets (enlarged images are shown in Fig. S1), the thickness of the MnO_2 nanosheets layer increases with increasing the $KMnO_4$ concentration. Therefore, by changing $KMnO_4$ concentration 3D

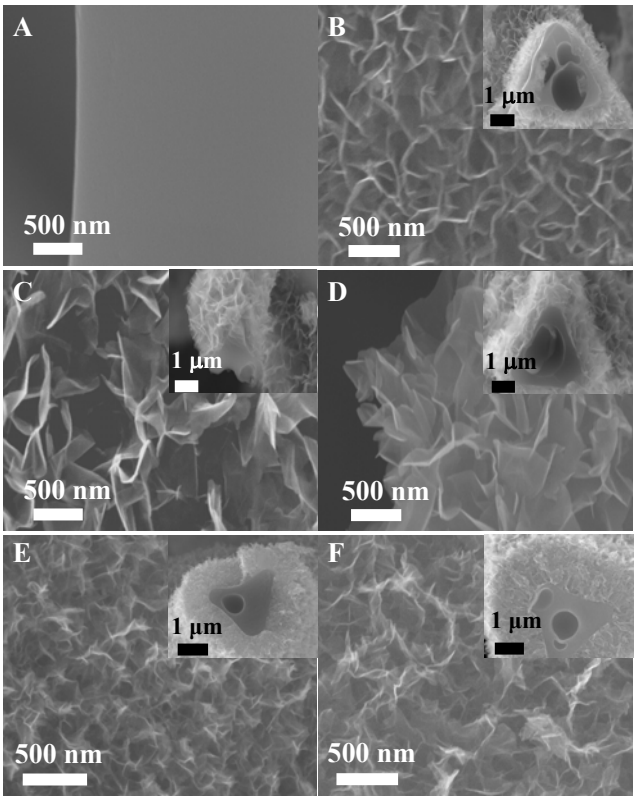

Fig. 2 Top view SEM images of the as-prepared 3D porous nanomaterials, (A) CF, (B) MnO_2/CF0.5, (C) MnO_2/CF1, (D) MnO_2/CF2, (E) MnO_2/CF3 and (F) MnO_2/CF5. The insets show the corresponding cross section view SEM images.

MnO_2/CF nanocomposites with optimized structure and composites can be constructed.

The crystal structure of the MnO_2 nanosheets was characterized by high-resolution TEM (HRTEM) measurements. As showed in Fig. 3A, the MnO_2 nanosheets have numerous wrinkles and ripples and are only a few nanometers in thickness. Such porous structure can effectively improve the surface/interface area of MnO_2 nanocrystals and the solution diffusion among the interspaces of MnO_2 nanosheets, which is beneficial for the rapid response to analyte. The HRTEM image shown in Fig. 3B reveals that the MnO_2 nanosheets are actually composed of small MnO_2 nanocrystals. From each crystal, well-resolved lattice fringes with interplanar spacing of 0.25 nm can be observed, which can be indexed to the (101) plane of birnessite-type MnO_2.[50]

The X-ray energy dispersive spectroscopy (EDS) result shown in Fig. S2A demonstrates that the as-prepared composites mainly contain C, Mn, and O. Trace of K is probably from $KMnO_4$ since there is always a possibility of potassium ions co-existing in the MnO_2 matrix.[51] The crystalline structure of MnO_2 in the composites was identified by XRD measurements. As shown in Fig. S2B, for CF, there are two broad diffraction peaks with 2θ around 25° and 44°, which can be ascribed to the (002) and (100) planes of amorphous carbon.[52] For MnO_2/CF composites, except for the peaks from CF, new diffraction peaks can be observed with 2θ around 12°, 37° and 66°, corresponding

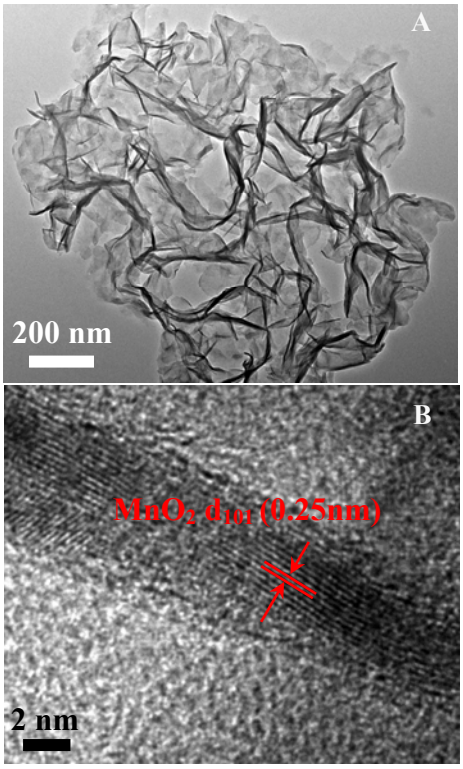

Fig. 3 (A, B) HRTEM images of the MnO_2 nanosheets stripped from MnO_2/CF0.5 at different magnifications.

to the (001), (111) and (020) diffraction of birnessite-type MnO_2 crystalline phase (JCPDS no.42-1317).[53] Meanwhile, with the increasing of $KMnO_4$ concentration in the synthesis, the diffraction peaks belonging to MnO_2 became stronger and the intensities of the diffraction peaks from CF decreased, indicating increased MnO_2 content from MnO_2/CF0.5 to MnO_2/CF5. The XPS survey on sample MCF0.5 is shown in Fig. S2C. The XPS signals of elements C, Mn and O could be seen clearly. Fig. S2D shows the Mn 2p core-level XPS spectrum. The binding energies of Mn $2p_{3/2}$ and $2p_{1/2}$ located at about 642.1 and 653.8 eV, respectively, with a spin-energy separation of 11.7 eV, suggesting the predominant oxidation state of Mn is +4.[54] Thermogravimetric analysis (TGA) was then performed to analyze the real composition of the products. From the results showed in Fig. S3, the weight percents of MnO_2 in MnO_2/CF0.5, MnO_2/CF1, MnO_2/CF2, MnO_2/CF3 and MnO_2/CF5 were calculated to be 7.7%, 10.9%, 24.5%, 47.9% and 66.9%, respectively.

3.2 Electrochemical sensing performance of 3D MnO_2/CF composites for H_2O_2 detection

3.2.1 Electrochemical response of MnO_2/CF electrode to H_2O_2

The electrochemical sensing performance of the MnO_2/CF composites with different size and thickness of MnO_2 nanosheets were evaluated by cyclic voltammetry (CV). Fig. 4A and B show the CV curves of the bare carbon foam (CF) and MnO_2/CF2 composite electrodes with the absence and presence of different concentrations of H_2O_2 in 0.1 M PBS (pH = 7.4), respectively. It can be seen that on the bare CF electrode, with the concentration

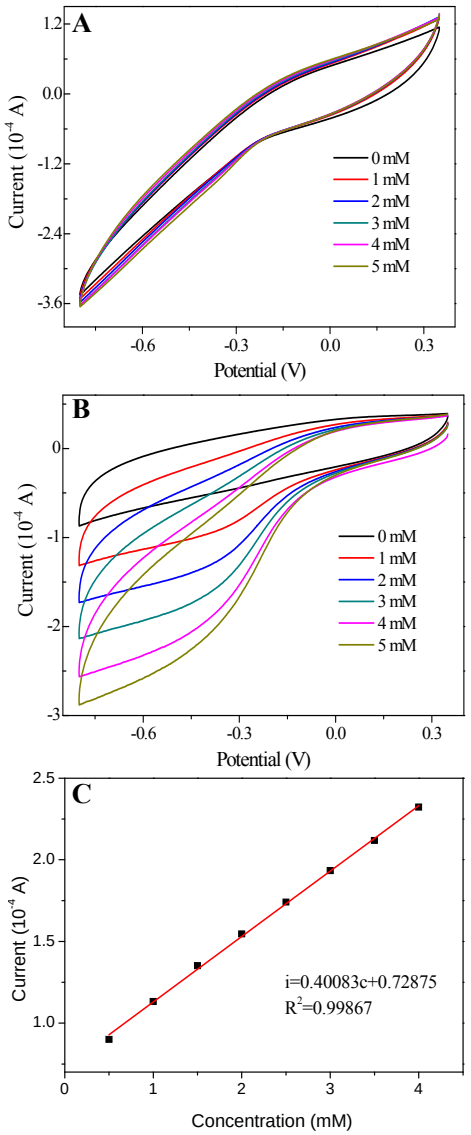

Fig. 4 CVs of bare CF (A), MnO_2/CF2 (B) in the absence and presence of H_2O_2 in 0.1 M PBS (pH=7.4) at a scan rate of 0.02 V/s. (C) The calibration curve of the reduction current dependent on H_2O_2 concentration obtained from Fig. 4B at -0.6 V.

of H_2O_2 increasing from 0 to 5 mM, the obtained CVs exhibited little change, indicating the negligible electrocatalytic activity of carbon foam for H_2O_2 reduction. Compared to the bare CF, obvious H_2O_2 reduction current can be observed on the MnO_2/CF2 composite electrode and the current increases with the increasing of H_2O_2 concentrations. As shown in Fig. 4C, the reduction current at -0.6 V exhibits a good linear relationship (R^2 = 0.999) with the H_2O_2 concentration, indicating the outstanding sensitivity of MnO_2 nanosheets to the concentration change of H_2O_2. The cyclic voltammogram tests demonstrate that the response current of MnO_2/CF composite electrodes to H_2O_2 is mainly from the MnO_2 nanosheets and CF only serves as a conductive backbone. Fig. S4 shows the CVs of H_2O_2 reduction on the other MnO_2/CF composite electrodes. Similar to the MnO_2/CF2, all the MnO_2/CF electrodes exhibit electrochemical response to the addition of H_2O_2. Such CV results indicate that

the formed MnO_2 nanosheets on the carbon foam have electrocatalytic activity for H_2O_2 reduction and the 3D MnO_2/CF composites could be used as electrochemical sensing platform for H_2O_2 detection.

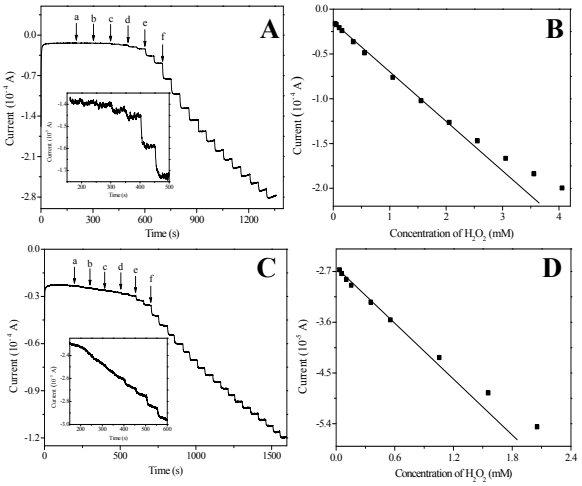

Fig. 5 The amperometric response of the MnO_2/CF2 (A) and MnO_2/CF5 (C) electrodes to H_2O_2, 10 μL 7.5 mM, 15 mM, 60 mM, 0.15 M, 0.6 M and 1.5 M H_2O_2 were added into the PBS at a, b, c, d, e, f, respectively. Insets in (A) and (C) are the amperometric response from low H_2O_2 concentration range at the corresponding electrodes, respectively. (B, D) The corresponding plots of the response current *vs.* H_2O_2 concentration obtained from the MnO_2/CF2 (B) and MnO_2/CF5 (D) electrodes, respectively.

By comparing the CVs on the MnO_2/CF composites with different MnO_2 contents, the onset potentials of H_2O_2 reduction are different. For the MnO_2/CF0.5, MnO_2/CF3 and MnO_2/CF5 samples, the onset potentials are close to or more negative than 0.0 V. However, the onset potentials observed from the MnO_2/CF1 and MnO_2/CF2 electrodes are much more positive than 0.0 V (around 0.15 V). Therefore, the MnO_2 content covered on the carbon foam have large effect on the electrocatalytic activity and the MnO_2/CF1 and MnO_2/CF2 composites exhibit the optimized composition for H_2O_2 reduction. From the SEM images shown in Fig. 2 insets and Fig. S1, too thin and too thick MnO_2 layers were formed on the MnO_2/CF0.5, MnO_2/CF3 and MnO_2/CF5 composites. However, the MnO_2/CF1 and MnO_2/CF2 exhibit a moderate thickness of MnO_2 layers. Moreover, compared to other composites, the MnO_2/CF1 and MnO_2/CF2 are covered by larger MnO_2 nanosheest (Fig. 2), suggesting the larger pores formed in the two porous structures. The moderate thickness of MnO_2 nanosheets and the large pores in the MnO_2/CF1 and MnO_2/CF2 structures are beneficial for the electrical conductivity and mass transport during electrochemical reactions, resulting in the higher electrochemical performance for H_2O_2 reduction. By comparing Fig. 4B and Fig. S4B, one can see that curent from MnO_2/CF3 is larger than that from MnO_2/CF2 electrode. It should be noted that the currents shown in Fig.4 and Fig. S4 are not normalized to the mass loading of MnO_2 on the electrodes. In fact, the weights of the MnO_2/CF electrodes increase with the increasing of MnO_2 mass ratio in the MnO_2/CF composites. In order to compare the performances of MnO_2/CF2 and MnO_2/CF3, the CVs of the two electrodes with response currents normalized to the weight of MnO_2 were shown in Fig S5. It is clear that the normilized current response from MnO_2/CF2 is larger than that of MnO_2/CF3. Based on above electrochemical results, MnO_2/CF2 is mainly selected in the following studies for H_2O_2 detection.

3.2.2 Amperometric response of the MnO_2/CF electrodes to H_2O_2

In a typical hydrogen peroxide sensing experiment, 10 μL H_2O_2 solution with different concentrations (7.5 mM, 15 mM, 60 mM, 0.15 M, 0.6 M and 1.5 M) was successively injected into the stirring electrolyte solution (0.1 M PBS, pH = 7.4) at room temperature at a potential of -0.45 V. The background current was allowed to decay to a constant value before H_2O_2 solution was added to the cell. It was observed that the MnO_2/CF2 electrode responded quickly to the change of H_2O_2 concentration and reached a steady-state signal within 10 s (Fig. 5A). The corresponding calibration curve for the H_2O_2 detection is shown in Fig. 5B. The sensor displays a linear range from 2.5 μM to 2.06 mM (R = 0.999), and a detection limit of 1.2×10^{-7} M (signal/noise = 3). For comparison, the amperometric response of the MnO_2/CF5 towards the reduction of H_2O_2 and the corresponding calibration curve are shown in Fig. 5C and D. The linear range for H_2O_2 detection is from 35 μM to 0.56 mM and the detection limit is estimated to be 3.1×10^{-5} M. By comparing the insets in Fig. 5A and B, at low H_2O_2 concentrations, the MnO_2/CF2 still have sensitive amperometric responses. However, only unresolvable currents were observed on the MnO_2/CF5 composite upon the addition of different concentrations of H_2O_2. Obviously, in comparison with the MnO_2/CF5 composite, the MnO_2/CF2 exhibits a much higher electrochemical sensing performance for H_2O_2 with a wider linear range and lower detection limit. The amperometric responses of the other MnO_2/CF electrodes to H_2O_2 and the corresponding calibration curves are shown in Fig. S6.

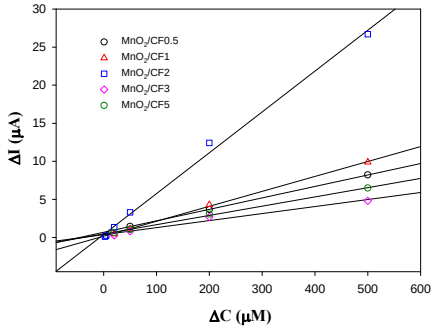

Fig. 6 Current responses of the MnO_2/CF composites to the change of H_2O_2 concentrations. Data were obtained from Fig. 4B and Fig. S4.

To compare the sensitivity of the MnO_2/CF composites for H_2O_2 detection, Fig. 6 shows the plots of current change dependence on the concentration change of hydrogen peroxide at the five electrodes. Obviously, all the MnO_2/CF composites show linear current responses to H_2O_2 concentrations, again suggesting the good response of the MnO_2/CF-based H_2O_2 sensors. Moreover, the largest slope of the plots was obtained from the MnO_2/CF2 electrode, indicating the highest sensitivity of the

MnO_2/CF2 sample. The comparison of the detection performance obtained from the 3D MnO_2/CF materials is summarized in Table 1. It can be seen that the sensitivity of the MnO_2/CF electrodes to H_2O_2 increases with MnO_2 content below 24.5% (the MnO_2 content in MnO_2/CF2). Further increase of MnO_2 content above 24.5% leads to decreased sensitivity and narrower linear range. Thus, the MnO_2/CF2 exhibited the best sensing performance for H_2O_2 detection. Such performance change agrees well with the results of electrocatalytic activity obtained from CV measurements (Fig. 4 and S4). The decreased detection performance with high content of MnO_2 could be mainly attributed to the intrinsic low electric conductivity of the thick MnO_2 layers.

Table 1 Comparison of the performance of various H_2O_2 sensors based on MnO_2/CF composites

Samples	MnO_2 $\%_{wt}$	Linear range (μM)	Detection limit (M)	Sensitivity (μA/μM)
MnO_2/CF0.5	7.7%	1.05×10^{-5} to 2.06×10^{-3}	1.0×10^{-6}	0.015
MnO_2/CF1	10.9%	3.5×10^{-5} to 3.56×10^{-3}	1.6×10^{-7}	0.020
MnO_2/CF2	24.5%	2.5×10^{-6} to 2.06×10^{-3}	1.2×10^{-7}	0.054
MnO_2/CF3	47.9%	3.5×10^{-5} to 1.06×10^{-3}	2.1×10^{-6}	0.009
MnO_2/CF5	66.9%	3.5×10^{-5} to 5.55×10^{-4}	3.1×10^{-5}	0.012

Table 2 Comparison of the performance of electrochemical H_2O_2 sensors based on various mateials.

Samples	Linear range(M)	Detection limit(M)	Ref.
Fe_3O_4/MWCNT	6.0×10^{-5} to 3.6×10^{-4}	1×10^{-5}	55
CoOOH nanosheets	4.0×10^{-5} to 1.6×10^{-3}	4×10^{-5}	56
CoO_xNPs/ERGO	5.0×10^{-6} to 1.0×10^{-3}	2×10^{-7}	57
Cu-NPs/PoPD	1.0×10^{-6} to 1.0×10^{-3}	1×10^{-7}	58
Pd/PEDOT	2.5×10^{-6} to 1.0×10^{-3}	2.84×10^{-7}	59
$Ni(OH)_2$/MWCNT	1.5×10^{-6} to 2.5×10^{-3}	6.1×10^{-7}	60
Urchin-like core-shell CuO	1.0×10^{-5} to 5.55×10^{-3}	/	61
MnO_2 microspheres/Nafion	1.0×10^{-5} to 1.5×10^{-4}	2×10^{-6}	62
MnO_x nanoparticles	2.0×10^{-5} to 1.26×10^{-3}	2×10^{-5}	31
MnO_2 nanosheets/chitosan	5.0×10^{-6} to 3.5×10^{-3}	1.5×10^{-6}	63
Mn-NTA nanowires	5.0×10^{-6} to 2.5×10^{-3}	2×10^{-7}	64
MnO_2 nanorods	1.0×10^{-6} to 1.5×10^{-3}	1×10^{-7}	65
MnO_2/VACNTs	1.2×10^{-6} to 1.8×10^{-3}	8.0×10^{-7}	37
MnO_2/graphene/CNT	1×10^{-6} to 1.03×10^{-3}	1×10^{-7}	66
MnO_2/GO	5×10^{-6} to 6×10^{-4}	8.0×10^{-7}	67
MnO_2/CF2	2.5×10^{-6} to 2.055×10^{-3}	1.2×10^{-7}	This work

To further study the charge transfer resistance of the MnO_2/CF-based H_2O_2 sensors, electrochemical impedance spectroscopy results from different samples were collected and compared, as shown in Fig. S7. The diameter of the semicircle at high frequency corresponds to the charge transfer resistance (R_{ct}) at the interface where reaction takes place, involving both ion and electron transfer processes. Note that the R_{ct} increases with the increase of MnO_2 content in the composites which is ascribed to the intrinsic low electric conductivity of MnO_2. For comparison, the electrochemical sensing performance of MnO_2/CF2 and other reported materials for H_2O_2 detection are listed in Table 2. It can be seen that the present MnO_2/CF2 shows better or at least comparable performance compared to the other electrochemical sensing materials. The good performance of MnO_2/CF2 could be attributed to following reasons. First, the 3D interconnected carbon foam scaffold provides a high conductive backbone for epitaxial growth of MnO_2 nanosheets which favors the electron transfer and thus guarantees the full utilization of MnO_2 nanosheets. Second, the hierarchical porous structure of the hybrid networks, including the micro-sized macropores of carbon foam and the nano-sized interspace among MnO_2 nanosheets, is favorable for electrolyte immersion and diffusion. Finally, the ultrathin and wrinkled structure of MnO_2 nanosheets is beneficial for preventing aggregation of MnO_2 nanosheets and improving their available surface area to analyte. Here, we also compared the detection performance with those of non-electrochemical H_2O_2 sensors. It was found that our results are comparable to those obtained by other non-electrochemical detection methods. For instance, carbon dots derived from β-cyclodextrin are capable of detecting H_2O_2 in the linear range from 2.0×10^{-6} M to

5.0×10^{-4} M with the detection limit of 1.0×10^{-6} M via colorimetric detection method.[68] In another report,[69] a TiO_2/SiO_2 composite prepared by a sol−gel route showed a linear response to H_2O_2 concentration ranging from 7.0×10^{-6} to 7.0×10^{-2} M by a phosphorescence method.

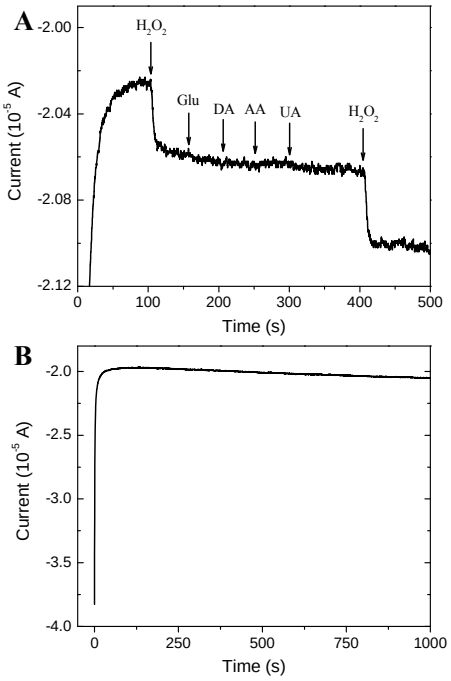

Fig. 7 (A) Interference experiments of glucose (Glu), dopamine (DA), ascorbic acid (AA), uric acid (UA) for the H_2O_2 sensing on the MnO_2/CF2-based sensor in 0.1 M PBS (pH=7.4) at -0.45V. The concentration of analytes are: H_2O_2 50 μM, Glu 100 μM, DA 100 μM, AA 100 μM and UA 100 μM. (B) Stability test of the MnO_2/CF2-based sensor in 0.1 M PBS (pH=7.4) at -0.45 V (vs Ag/AgCl).

3.2.3 Interferences and stability

The possible interference of foreign chemicals, which might exist in real samples, was investigated during the amperometric determination of H_2O_2. The interference experiments were performed in 0.1 M PBS (pH=7.4) at -0.45 V by comparing the amperometric response from H_2O_2 (50 μM) and twofold concentrations of each interfering substance of glucose (Glu), dopamine (DA), ascorbic acid (AA), and uric acid (UA). The amperometric responses of the MnO_2/CF2 towards the different analytes are showed in Fig. 7A. It can be seen that twofold concentration of Glu, DA, AA and UA shows negligible current changes compared to that of H_2O_2. Such result indicates the remarkable anti-interference properties of the MnO_2/CF2-based sensor to Glu, DA, AA and UA. The stability of the MnO_2/CF2 sensor was evaluated by measuring the amperometric response at -0.45 V in 0.1 M PBS. As displayed in Fig. 7B, only a little current change can be observed during 1000 s test period, indicating the high stability of the MnO_2/CF2 sensor.

4. Conclusions

In summary, a type of nonenzymatic electrochemical sensors based on 3D porous MnO_2/CF composite were fabricated by in-situ deposition of MnO_2 nanosheets on the surface of carbon foam. Structural characterizations clearly demonstrated the formation of porous MnO_2 nanosheet layers on the 3D carbon framework. It was found that the size of the MnO_2 nanosheet and the thickness of the MnO_2 composite depend strongly on the content of MnO_2. The sensors fabricated from the 3D MnO_2/CF nanostructures exhibited a MnO_2 content-dependent sensing performance for H_2O_2 detection. The MnO_2/CF2 with 24.5% MnO_2 content exhibited the highest performance among the studied materials with low detection limit, high sensitivity, wide linear range, good selectivity and stability. The excellent sensing properties of the 3D MnO_2/CF hybrids could be attributed to the high conductivity from carbon backbone, improved mass transport from the porous structure and the high electrocatalytic activity of the thin MnO_2 nanosheets. Therefore, the catalytic nature of MnO_2 towards H_2O_2 reduction, combined with the high conductive carbon network make the 3D MnO_2/CF composites hold the promise for the development of nonenzymatic sensor at a low cost.

Acknowledgements

This work was supported by the National Natural Science Foundation of China (No. 21275136) and the Natural Science Foundation of Jilin province, China (No. 201215090).

Notes and references

[a] *State Key Laboratory of Electroanalytical Chemistry, Changchun Institute of Applied Chemistry, Chinese Academy of Sciences, Changchun 130022, Jilin, China. Tel: +86431-85262723; E-mail: weichen@ciac.ac.cn*

[b] *University of Chinese Academy of Sciences, Beijing 100039, China*

† Electronic Supplementary Information (ESI) available: Additional structural characterizations and electrochemical measurements. See DOI: 10.1039/b000000x/

1. Y. Q. Miao and S. N. Tan, *Analyst*, 2000, **125**, 1591-1594.
2. S. S. Razola, B. L. Ruiz, N. M. Diez, H. B. Mark and J. M. Kauffmann, *Biosens. Bioelectron.*, 2002, **17**, 921-928.
3. B. Q. Wang, B. Li, Z. X. Wang, G. B. Xu, Q. Wang and S. J. Dong, *Anal. Chem.*, 1999, **71**, 1935-1939.
4. M. M. Liu, R. Liu and W. Chen, *Biosens. Bioelectron.*, 2013, **45**, 206-212.
5. M. J. Song, S. W. Hwang and D. Whang, *Talanta*, 2010, **80**, 1648-1652.
6. D. W. Kimmel, G. LeBlanc, M. E. Meschievitz and D. E. Cliffel, *Anal. Chem.*, 2012, **84**, 685-707.
7. F. G. Xu, Y. J. Sun, Y. Zhang, Y. Shi, Z. W. Wen and Z. Li, *Electrochem. Commun.*, 2011, **13**, 1131-1134.
8. X. J. Bo, J. Bai, L. X. Wang and L. P. Guo, *Talanta*, 2010, **81**, 339-345.
9. Y. Shi, Z. L. Liu, B. Zhao, Y. J. Sun, F. G. Xu, Y. Zhang, Z. W. Wen, H. B. Yang and Z. Li, *J. Electroanal. Chem.*, 2011, **656**, 29-33.
10. S. Palanisamy, S. M. Chen and R. Sarawathi, *Sensor. Actuat. B-Chem.*, 2012, **166**, 372-377.
11. K. M. Liao, P. Mao, Y. H. Li, Y. L. Nan, F. Q. Song, G. H. Wang and M. Han, *Sensor. Actuat. B-Chem.*, 2013, **181**, 125-129.
12. W. W. He, X. C. Wu, J. B. Liu, K. Zhang, W. G. Chu, L. L. Feng, X. N. Hu, W. Y. Zhou and S. S. Xie, *Langmuir*, 2010, **26**, 4443-4448.
13. W. Zhao, H. C. Wang, X. Qin, X. S. Wang, Z. X. Zhao, Z. Y. Miao, L. L. Chen, M. M. Shan, Y. X. Fang and Q. Chen, *Talanta*, 2009, **80**, 1029-1033.
14. A. S. Rad, A. Mirabi, E. Binaian and H. Tayebi, *Int. J. Electrochem. Sc.*, 2011, **6**, 3671-3683.
15. S. J. Guo, D. Wen, Y. M. Zhai, S. J. Dong and E. K. Wang, *Acs Nano*, 2010, **4**, 3959-3968.

16. Y. X. Fang, S. J. Guo, C. Z. Zhu, Y. M. Zhai and E. K. Wang, *Langmuir*, 2010, **26**, 11277-11282.
17. J. S. Huang, D. W. Wang, H. Q. Hou and T. Y. You, *Adv. Funct. Mater.*, 2008, **18**, 441-448.
18. Y. G. Li, B. Tan and Y. Y. Wu, *J. Am. Chem. Soc.*, 2006, **128**, 14258-14259.
19. C.-C. Kuo, W.-J. Lan and C.-H. Chen, *Nanoscale*, 2014, **6**, 334-341.
20. W. J. Lan, C. C. Kuo and C. H. Chen, *Chem. Commun.*, 2013, **49**, 3025-3027.
21. L. Lu and X. R. Huang, *Microchim. Acta*, 2011, **175**, 151-157.
22. B. J. Wang, L. Q. Luo, Y. P. Ding, D. S. Zhao and Q. L. Zhang, *Colloid. Surface. B*, 2012, **97**, 51-56.
23. M. S. Lin and H. J. Len, *Electroanal.*, 2005, **17**, 2068-2073.
24. L. C. Jiang and W. D. Zhang, *Electroanal.*, 2009, **21**, 988-993.
25. H. L. Hsu, J. M. Jehng and Y. C. Liu, *Mater. Chem. Phys.*, 2009, **113**, 166-171.
26. Z. X. Zhang, H. Zhu, X. L. Wang and X. R. Yang, *Microchim. Acta*, 2011, **174**, 183-189.
27. J. Bai and X. Jiang, *Anal. Chem.*, 2013, **85**, 8095-8101.
28. T. Y. Wang, H. C. Zhu, J. Q. Zhuo, Z. W. Zhu, P. Papakonstantinou, G. Lubarsky, J. Lin and M. X. Li, *Anal. Chem.*, 2013, **85**, 10289-10295.
29. H. M. Chen, J. H. He, C. B. Zhang and H. He, *J. Phys. Chem. C*, 2007, **111**, 18033-18038.
30. X. S. Yang, X. Chen, X. Zhang, W. S. Yang and D. G. Evans, *Sensor. Actuat. B-Chem.*, 2008, **129**, 784-789.
31. S. Thiagarajan, T. H. Tsai and S. M. Chen, *Int. J. Electrochem. Sc.*, 2011, **6**, 2235-2245.
32. S. J. Yao, S. Yuan, J. H. Xu, Y. Wang, J. L. Luo and S. S. Hu, *Appl. Clay. Sci.*, 2006, **33**, 35-42.
33. X. W. Zheng and Z. H. Guo, *Talanta*, 2000, **50**, 1157-1162.
34. C. E. Langley, B. Sljukic, C. E. Banks and R. G. Compton, *Anal. Sci.*, 2007, **23**, 165-170.
35. X. H. Cao, Z. Y. Zeng, W. H. Shi, P. R. Yep, Q. Y. Yan and H. Zhang, *Small*, 2013, **9**, 1703-1707.
36. L. Q. Luo, F. Li, L. M. Zhu, Z. Zhang, Y. P. Ding and D. M. Deng, *Electrochim. Acta*, 2012, **77**, 179-183.
37. B. Xu, M. L. Ye, Y. X. Yu and W. D. Zhang, *Anal. Chim. Acta*, 2010, **674**, 20-26.
38. X. P. Xiao, Y. H. Song, H. Y. Liu, M. Y. Xie, H. Q. Hou, L. Wang and Z. Li, *J. Mater. Sci.*, 2013, **48**, 4843-4850.
39. X. Lu, X. Xiao, Z. Li, F. Xu, H. Tan, L. Sun and L. Wang, *Anal. Methods*, 2014, **6**, 235-241.
40. F. Xiao, Y. Q. Li, H. C. Gao, S. B. Ge and H. W. Duan, *Biosens. Bioelectron.*, 2013, **41**, 417-423.
41. X. C. Dong, Y. W. Ma, G. Y. Zhu, Y. X. Huang, J. Wang, M. B. Chan-Park, L. H. Wang, W. Huang and P. Chen, *J. Mater. Chem.*, 2012, **22**, 17044-17048.
42. X. C. Dong, H. Xu, X. W. Wang, Y. X. Huang, M. B. Chan-Park, H. Zhang, L. H. Wang, W. Huang and P. Chen, *Acs Nano*, 2012, **6**, 3206-3213.
43. D. Y. Zhai, B. R. Liu, Y. Shi, L. J. Pan, Y. Q. Wang, W. B. Li, R. Zhang and G. H. Yu, *Acs Nano*, 2013, **7**, 3540-3546.
44. X. Cao, Z. Zeng, W. Shi, P. Yep, Q. Yan and H. Zhang, *Small*, 2013, **9**, 1703-1707.
45. T. Y. Wang, Z. Peng, Y. H. Wang, J. Tang and G. F. Zheng, *Sci. Rep.*, 2013, **3**.
46. C. C. Kung, P. Y. Lin, F. J. Buse, Y. H. Xue, X. Yu, L. M. Dai and C. C. Liu, *Biosens. Bioelectron.*, 2014, **52**, 1-7.
47. L. Li, M. M. Liu, S. J. He and W. Chen, *Anal. Chem.*, 2014, **86**, 7996-8002.
48. M. M. Liu, S. J. He and W. Chen, *Nanoscale*, 2014, DOI**:** 10.1039/C4NR03043E.
49. F. N. Xi, D. J. Zhao, X. W. Wang and P. Chen, *Electrochem. Commun.*, 2013, **26**, 81-84.
50. Y. S. Luo, J. Jiang, W. W. Zhou, H. P. Yang, J. S. Luo, X. Y. Qi, H. Zhang, D. Y. W. Yu, C. M. Li and T. Yu, *J. Mater. Chem.*, 2012, **22**, 8634-8640.
51. G. X. Zhao, J. X. Li, L. Jiang, H. L. Dong, X. K. Wang and W. P. Hu, *Chem. Sci.*, 2012, **3**, 433-437.
52. M. Y. Zhang, C. L. Shao, J. B. Mu, X. M. Huang, Z. Y. Zhang, Z. C. Guo, P. Zhang and Y. C. Liu, *J. Mater. Chem.*, 2012, **22**, 577-584.
53. S. B. Ma, K. Y. Ahn, E. S. Lee, K. H. Oh and K. B. Kim, *Carbon*, 2007, **45**, 375-382.
54. J. T. Zhang and X. S. Zhao, *Carbon*, 2013, **52**, 1-9.
55. X. B. Hu and C. Y. Wang, *Microchim. Acta*, 2012, **179**, 329-335.
56. K. K. Lee, P. Y. Loh, C. H. Sow and W. S. Chin, *Biosens. Bioelectron.*, 2013, **39**, 255-260.
57. S. J. Li, J. M. Du, J. P. Zhang, M. J. Zhang and J. Chen, *Microchim. Acta*, 2014, **181**, 631-638.
58. S. A. Kumar, P. H. Lo and S. M. Chen, *J. Electrochem. Soc.*, 2009, **156**, E118-E123.
59. F. X. Jiang, R. R. Yue, Y. K. Du, J. K. Xu and P. Yang, *Biosens. Bioelectron.*, 2013, **44**, 127-131.
60. Y. Chang, J. Qiao, Q. L. Liu, L. Z. Shangguan, X. W. Ma, S. M. Shuang and C. A. Dong, *Anal. Lett.*, 2008, **41**, 3147-3160.
61. J. Y. Li, S. L. Xiong, J. Pan and Y. T. Qian, *J. Phys. Chem. C*, 2010, **114**, 9645-9650.
62. L. Zhang, Z. Fang, Y. H. Ni and G. C. Zhao, *Int. J. Electrochem. Sc.*, 2009, **4**, 407-413.
63. P. Zhang, D. Guo and Q. H. Li, *Mater. Lett.*, 2014, **125**, 202-205.
64. S. Liu, L. M. Li, Q. Y. Hao, X. M. Yin, M. Zhang, Q. H. Li, L. B. Chen and T. H. Wang, *Talanta*, 2010, **81**, 727-731.
65. K. J. Babu, A. Zahoor, K. S. Nahm, R. Ramachandran, M. A. J. Rajan and G. G. Kumar, *J. Nanopart. Res.*, 2014, **16**.
66. D. X. Ye, H. X. Li, G. H. Liang, J. Luo, X. X. Zhang, S. Zhang, H. Chen and J. L. Kong, *Electrochim. Acta*, 2013, **109**, 195-200.
67. L. Li, Z. Du, S. Liu, Q. Hao, Y. Wang, Q. Li and T. Wang, *Talanta*, 2010, **82**, 1637-1641.
68. W. F. Zhu, J. Zhang, Z. C. Jiang, W. W. Wang and X. H. Liu, *Rsc Adv*, 2014, **4**, 17387-17392.
69. X. H. Shu, Y. Chen, H. Y. Yuan, S. F. Gao and D. Xiao, *Anal. Chem.*, 2007, **79**, 3695-3702.